RAA 2021 Vol. **21** No. **1**, 6(14pp) doi: 10.1088/1674-4527/21/1/6

http://www.raa-journal.org *http://iopscience.iop.org/raa*

***R**esearch in*
***A**stronomy and*
***A**strophysics*

Spatially-resolved stellar population properties of the M51–NGC 5195 system from multi-wavelength photometric data

Peng Wei[1,2,3,4], Hu Zou[3,4], Lin Lin[5], Xu Zhou[3,4], Xiang Liu[1], Xu Kong[6], Lu Ma[1] and Shu-Guo Ma[1,2]

[1] Xinjiang Astronomical Observatory, Chinese Academy of Sciences, Urumqi 830011, China; *weipeng@xao.ac.cn*
[2] School of Astronomy and Space Science, University of Chinese Academy of Sciences, Beijing 101408, China
[3] CAS Key Laboratory of Optical Astronomy, National Astronomical Observatories, Chinese Academy of Sciences, Beijing 100101, China; *zouhu@nao.cas.cn*
[4] Center for Astronomical Mega-Science, Chinese Academy of Sciences, Beijing, 100012, China
[5] Shanghai Astronomical Observatory, Chinese Academy of Sciences, Shanghai 200030, China
[6] Key Laboratory for Research in Galaxies and Cosmology, Department of Astronomy, University of Science and Technology of China, Hefei 230026, China

Received 2020 January 16; accepted 2020 July 13

Abstract Using multi-band photometric images of M51 and its companion NGC 5195 from ultraviolet to optical and infrared, we investigate spatially resolved stellar population properties of this interacting system with stellar population synthesis models. The observed infrared excess (IRX) is used to constrain dust extinction. Stellar mass is also inferred from the model fitting. By fitting observed spectral energy distributions (SEDs) with synthetical ones, we derive two-dimensional distributions of stellar age, metallicity, dust extinction and stellar mass. In M51, two grand-designed spiral arms extending from the bulge show young age, rich metallicity and abundant dust. The inter-arm regions are filled with older, metal-poorer and less dusty stellar populations. Except for the spiral arm extending from M51 into NGC 5195, the stellar population properties of NGC 5195 are quite featureless. NGC 5195 is much older than M51, and its core is very dusty with A_V up to 1.67 mag and dense in stellar mass surface density. The close encounters might drive the dust in the spiral arm of M51 into the center of NGC 5195.

Key words: galaxies: evolution — galaxies: individual (M51) — galaxies: photometry

1 INTRODUCTION

Understanding how galaxies have evolved into their present-day forms is one of the foremost goals in extragalactic astronomy. At present, the evolution of local galaxies might be in transition from hierarchical clustering and merging in the early universe to secular processes in the future (Kormendy & Kennicutt 2004). Hierarchical clustering and merging processes are rapid and violent and can account remarkably well for large-scale structures in the cosmological Λ cold dark matter (Λ-CDM) models (White & Rees 1978). For nearby galaxies, there have been a considerable number of studies on the galaxy formation and evolution induced by some secular processes, gas-rich accretion events, gravitational encounters, and gravitational interactions with satellite galaxies (Toomre & Toomre 1972; Kormendy & Kennicutt 2004; Cortés et al. 2006; Fisher & Drory 2008; Roškar et al. 2008; Fisher et al. 2009; Fisher & Drory 2010; Kormendy et al. 2010).

Nearby galaxies provide ideal astrophysical laboratories to study galaxy formation and evolution in sub-galactic scales, both observationally and theoretically (Dobbs et al. 2010). There are substantial multi-band archival data from various surveys and telescopes, such as the Galaxy Evolution Explorer (GALEX; Martin et al. 2005), Sloan Digital Sky Survey (SDSS; York et al. 2000), Beijing-Arizona-Taiwan-Connecticut (BATC) Multicolor Sky Survey (Burstein et al. 1994), Two Micron All Sky Survey (2MASS; Jarrett et al. 2003), Spitzer Space Telescope (Werner et al. 2004; Kennicutt et al. 2003), Herschel Very Nearby Galaxies Survey (VNGS; Mentuch Cooper et al. 2012) and The HI Nearby Galaxy Survey (THINGS; Walter et al. 2008). Multi-wavelength data from ultraviolet (UV) to radio, which contain abundant information on stellar, gas and dust contents, can help us to understand galaxy evolution.

As evolutionary population synthesis (EPS) models become more and more popular and mature

(Fioc & Rocca-Volmerange 1997; Leitherer et al. 1999; Bruzual & Charlot 2003; Kotulla et al. 2009), multi-band photometric data have been utilized to accurately derive physical properties of underlying stellar populations, such as stellar age, metallicity and dust extinction. Based on the assumption that stars in a small region formed in an instantaneous burst that can be modeled as a simple stellar population (SSP), Kong et al. (2000) employed 13 BATC intermediate-band images of M81 and SSP models of GISSEL96 (Charlot & Bruzual A 1991; Bruzual A. & Charlot 1993) to derive two-dimensional age and reddening distributions. In this study, one BATC near-infrared (IR) color was used to estimate the metallicity. However, galaxies are much more complex systems than SSPs. Composite stellar populations (CSPs) assuming a proper star formation history (SFH) should be more accurate to model observational features of galaxies. Li et al. (2004a,b) utilized the PEGASE CSP models (Fioc & Rocca-Volmerange 1997) with exponentially decreasing star formation rate (SFR) to analyze the stellar population properties of M81 and M33. They obtained reasonable age maps of these two galaxies based on images of a broad U band and 13 intermediate bands from the BATC survey. Zou et al. (2011) and Lin et al. (2013) utilized the UV-to-IR spectral energy distributions (SEDs) and BC03 models (Bruzual & Charlot 2003) to analyze spatially resolved stellar population properties of NGC 628 and M101. Furthermore, the empirical infrared excess (IRX)-A_{FUV} relation was used to constrain the dust extinction in Lin et al. (2013). In these studies, they derived reliable two-dimensional maps of age, metallicity, dust reddening, and corresponding radial profiles. Both NGC 628 and M101 were reported to have features of pseudobulges and secular evolution.

In our previous works, we analyzed the detailed two-dimensional stellar population properties for several relatively isolated galaxies. This paper aims to study an interacting galaxy pair of M51 and NGC 5195. M51 (NGC 5194, the Whirlpool Galaxy) is a grand-design face-on spiral galaxy with Hubble type of Sbc. It has an inclination angle of about 20° and a distance of about 8.4 Mpc (Feldmeier et al. 1997). NGC 5195 is a post-starburst galaxy, which has no recent star formation (Mentuch Cooper et al. 2012). It was found that these two galaxies underwent a close encounter about 300–500 Myr ago by kinematical and hydrodynamical simulations (Salo & Laurikainen 2000; Dobbs et al. 2010). Through stellar population synthesis modeling, Mentuch Cooper et al. (2012) also found that M51 and NGC 5195 underwent a burst of star formation roughly 370–480 Myr ago, which is consistent with the simulations. In their study, they focused on the dust properties derived from mid- and far-IR data and meanwhile obtained the spatially-resolved distributions of stellar population properties, such as age, metallicity, dust extinction and star formation timescale. However, the determination of stellar population properties in Mentuch Cooper et al. (2012) was based on only seven bands, including four optical bands and three near-IR bands. Besides, two components of star formation histories were adopted. Therefore, the parameter degeneracy might be relatively serious. For example, they claimed that their dust extinction was modestly underestimated.

The M51-NGC 5195 system was observed with the BATC 15 intermediate-band filters. The intermediate color can be utilized to constrain the metallicity well (Kong et al. 2000). In addition, there are abundant archival multi-wavelength photometric data ranging from UV to IR. A total of 26 bands are gathered with wavelength ranging from 1500 Å to 4.5 μm. These bands are dominated by starlight and are used to derive the stellar population properties. The wide wavelength coverage and the dust constraint by adopting the IRX as exploited by Lin et al. (2013) help to degrade the parameter degeneracy significantly. We can also get higher spatial-resolution maps of those properties (about $6''$ or 240 pc, while $\sim$1 kpc in Mentuch Cooper et al. (2012)) and thus study the interacting system in more details. Through the derived distributions of the stellar population properties, we try to probe evolutionary clues of the M51-NGC 5195 system and investigate possible influence of the galactic interaction.

The outline of this paper is as follows. Section 2 introduces the multi-wavelength data and related image processing. Section 3 describes the stellar population synthesis models and corresponding SED fitting method. The parameter uncertainty and test of the parameter degeneracy are analyzed in this section. Section 4 presents the distributions of stellar population properties and Section 5 provides some discussions. Section 6 gives a summary.

2 MULTI-WAVELENGTH DATA AND IMAGE PROCESSING

Multi-wavelength photometric images of M51 and NGC 5195 are collected from a series of surveys and telescopes. A total of 28 images are used in this paper, including two UV bands from GALEX, one UV band from XMM Optical/UV Monitor (XMM-OM), 15 BATC intermediate bands, three broad-bands from Beijing-Arizona Sky Survey (BASS; Zou et al. 2017a) and Mayall z-band Legacy Survey (MzLS; Silva et al. 2016), three near-IR bands from 2MASS, and four near- and mid-IR bands from Spitzer. GALEX far-UV (FUV) and Spitzer mid-IR images are utilized to calculate dust extinction. The rest of the images are employed to derive the stellar population

Table 1 Information for Multi-band Data of M51-NGC 5195 Galaxy Pair

Name[a]	Filter	$\lambda_{\rm eff}$[b]	Bandwidth[c]	Pixel scale[d]	FWHM[e]	Calibration[f]	Reference[g]
GALEX	FUV	1516	268	1.5	4.85	0.05	(1)
	NUV	2267	732	1.5	5.52	0.03	
XMM-OM	UVW1	2905	620	0.95	2.67	0.03	(2)
BATC	*a-p*	3000–9900	120–310	1.7	3.2–4.8	0.03	(3)
BASS	*g*	4776	848	0.45	1.92	0.01	(4)
	r	6412	833	0.45	1.70	0.01	
MzLS	*z*	9203	826	0.26	1.20	0.01	(5)
2MASS	*J*	12350	1620	1.0	3.31	0.03	(6)
	H	16620	2510	1.0	3.25	0.03	
	K_s	21590	2620	1.0	3.35	0.03	
Spitzer	IRAC1	35500	7500	0.75	2.25	0.03	(7)
	IRAC2	44930	10100	0.75	2.27	0.03	
	IRAC4	78720	29300	0.75	2.65	0.03	
	MIPS24	237000	47000	2.5	6.0	0.03	

[a] Name of the survey or telescope; [b] Effective wavelength of each filter in Å; [c] Bandwidth of each filter in Å; [d] Pixel scale in arcsec; [e] FWHM of stars in arcsec; [f] Roughly estimated flux calibration accuracy in mag.
[g] References: (1) Morrissey et al. (2007); (2) Kuntz et al. (2008); (3) Zhou et al. (2001); (4) Zou et al. (2017a,b, 2018); (5) Silva et al. (2016); (6) Skrutskie et al. (2006); (7) Kennicutt et al. (2003).

Table 2 Filter Parameters for the BATC Photometric System and Observational Statistics of the M51 Field

No.	Filter	$\lambda_{\rm eff}$[a]	Bandwidth	Exposure[b]	FWHM[c]
1	a	3360	222	1080	4.88
2	b	3890	187	25200	4.45
3	c	4210	185	37500	4.03
4	d	4550	222	19200	4.17
5	e	4920	225	13200	4.09
6	f	5270	211	26400	4.13
7	g	5795	176	8400	3.43
8	h	6075	190	3600	4.53
9	i	6660	312	3600	4.25
10	j	7050	121	2700	3.99
11	k	7490	125	8400	3.81
12	m	8020	179	7200	4.00
13	n	8480	152	13200	3.63
14	o	9190	194	10800	3.37
15	p	9745	188	3600	4.82

[a] Effective wavelength in Å;
[b] Total exposure time in seconds;
[c] FWHM of stars in arcsec.

properties. Table 1 summarizes the information describing these data.

2.1 Ultraviolet Images

UV images come from GALEX (Martin et al. 2005) and XMM-OM (Mason et al. 2001). GALEX is a 50 cm Ritchey-Chrétien telescope and has two simultaneous channels of FUV and near-UV (NUV) with effective wavelengths at 1516 and 2267 Å, respectively. Deep images of M51 in these two bands were taken in 2007 with a total exposure time of 10 787 seconds by the Guest Investigator Program. These data are retrieved from the GALEX GR6/GR7 data release[1]. The XMM-OM is an optical/UV 30 cm telescope co-aligned with X-ray telescopes. It has a field of view of about 17′ and covers a wavelength range of 1600–6000 Å. The telescope has three UV filters, but M51 was observed in only the UVW1 band. The UVW1 mosaic can be obtained at MAST [2].

2.2 BATC Intermediate-band Images

M51 was observed by the 60/90 cm Schmidt telescope at the Xinglong Station of National Astronomical Observatories, Chinese Academy of Sciences, as part of the BATC sky survey. A description of this survey and the observing strategy can be found in Burstein et al. (1994). A 2048×2048 Ford Aerospace CCD camera with a pixel scale of $1''.7$ was mounted at the focal plane of the telescope. The field of view is about $58'$. The photometric system consists of 15 dedicated intermediate-band filters covering the wavelength range of 3300–10 000 Å with bandwidths of about 200–300 Å. These filters are designed well to avoid strong sky emission lines (Fan et al. 1996). Observations of the M51 field started in January 1995 and ended in July 2007. Normally, the individual exposure time was about 20 minutes. The raw images are processed by a data reduction pipeline customized for the BATC survey. The pipeline generates calibrated images with astrometric and photometric solutions tied to the UCAC3 catalog (Zacharias et al. 2010) and four Oke-Gunn standard stars (Oke & Gunn 1983), respectively. The standard stars were observed on photometric nights, giving a typical calibration accuracy of about 3%. The single-epoch images are aligned and stacked to create deep mosaics. Table 2 lists some observational statistics and filter parameters.

[1] http://galex.stsci.edu/GR6/

[2] http://archive.stsci.edu/index.html

2.3 Optical broad-band Images

M51/NGC 5195 is also observed by BASS and MzLS. These two surveys serve for the spectroscopic targeting of the Dark Energy Spectroscopic Instrument (DESI; Dey et al. 2019). The BASS relies on a wide-field camera of 90Prime deployed on the 2.3 m Bok telescope at Kitt Peak. The MzLS utilizes the MOSAIC-3 camera of the 4 m Mayall telescope on the same mountain. The photometric filters include g and r bands for BASS and z band for MzLS. These filters are very close to the ones employed by the Dark Energy Survey (DES; Dark Energy Survey Collaboration et al. 2016). There are three individual exposures for each filter. These individual CCD frames are reduced by the BASS pipeline (Zou et al. 2017b, 2018). The astrometric and photometric calibrations are respectively tied to the Gaia DR1 (Gaia Collaboration et al. 2016) and Pan-STARRS1 catalogs (Chambers et al. 2016). We stack individual images into deep mosaics by SWarp (Bertin 2010). The mosaics have a size of 5400×5400 pixels with a pixel scale is $0''.27$, which is close to the MOSAIC-3 CCD pixel size. The image qualities in point spread function (PSF) full width at half maximum (FWHM) as listed in Table 1 are $2''.0$, $1''.8$ and $1''.3$ for g, r and z bands, respectively.

2.4 Near/mid-infrared Images

The near-IR images of JHK_s bands with central wavelengths of 1.2, 1.65 and 2.2 μm are from the 2MASS Large Galaxy Atlas survey (Jarrett et al. 2003). The PSF FWHMs of 2MASS images are estimated to be about $3''.3$. Other IR observations come from the Spitzer Infrared Nearby Galaxies Survey (SINGS; Kennicutt et al. 2003). M51 was imaged by Spitzer with both Infrared Array Camera (IRAC at 3.6, 4.5, 5.6, 8.0 μm) and Multi-band Imaging Photometer (MIPS at 24, 70 and 160 μm). The PSF FWHM for IRAC is about $2''.0$ and that for MIPS is larger than $6''$.

2.5 Image Processing

Our goal is to analyze spatially resolved stellar population properties, so we need to uniformize the images from different telescopes (e.g., pixel scale and resolution). Here we describe the processing steps shortly (see more details in Zou et al. 2011; Lin et al. 2013). Firstly, the sky background is determined by a dedicated algorithm and subtracted from the mosaic for each band. The background map is a two-dimensional polynomial fitting of the background pixels after signals from objects and central large galaxies are removed. Secondly, all images are convolved to the MIPS 24 μm resolution (FWHM of about $6''$) with kernels estimated from the PSF profiles. Thirdly, all images are projected to the BATC i band with a pixel scale of $1''.7$. Fourthly, foreground bright stars identified from the 2MASS Point Source Catalog (Skrutskie et al. 2006) are masked.

Figure 1 features processed multi-wavelength images of the M51–NGC 5195 pair from different telescopes. UV and mid-IR emissions trace the star formation and dust distribution respectively. Near-IR bands are less affected by dust attenuation and can trace the stellar mass. From these images, the SED is extracted pixel by pixel. It is corrected for the Galactic extinction following the extinction law of Cardelli et al. (1989) and the reddening map of Schlegel et al. (1998) ($E(B-V)$ = 0.031).

3 STELLAR POPULATION MODELS AND SED FITTING METHOD

3.1 Spectral Models

The EPS has become a modern popular technique that can be applied for studying the stellar population properties of star clusters and galaxies. We can obtain a series of physical properties such as age, metallicity, intrinsic reddening, redshift, stellar mass and SFR by comparing observed spectra or photometric SEDs with model ones. Some popular stellar population synthesis models include PEGASE (Fioc & Rocca-Volmerange 1997), StarBurst99 (Leitherer et al. 1999), GALEXEV (Bruzual & Charlot 2003, hereafter BC03), Ma05 (Maraston 2005), CB07 (Bruzual 2007), BPASS (Eldridge & Stanway 2009), GALEV (Kotulla et al. 2009), etc.

The simplest EPS model is the SSP, which is composed of coeval stars with the same age and chemical composition. Providing an initial mass function (IMF) and stellar evolutionary tracks as well as stellar libraries, one can obtain the spectral evolution of an SSP. SSPs are suitable for star clusters and H II regions. However, galaxies are much more complex systems. An evolutionary CSP can more accurately describe the evolution history of a galaxy. The CSP is considered to be a superimposition of SSPs at different ages through assuming an SFH.

In this paper, we use the popular stellar population synthesis code BC03. The adopted parameter configurations include the Chabrier (2003) IMF, Padova 1994 evolutionary tracks and delayed-exponential SFH. The delayed-exponential SFH is expressed as $\psi(t) = \frac{t}{\tau^2}\exp\left(\frac{-t}{\tau}\right)$, where t is age and τ is the star formation timescale. As described in Lin et al. (2013), we construct a library of 10^5 CSP model spectra, which are randomly sampled in different parameter spaces of age, metallicity and τ. The age is uniformly sampled between 1 Myr and 13.5 Gyr. The metallicity is uniformly sampled between 0.2 and 2 $Z_{\odot}$. The star formation timescale τ is sampled

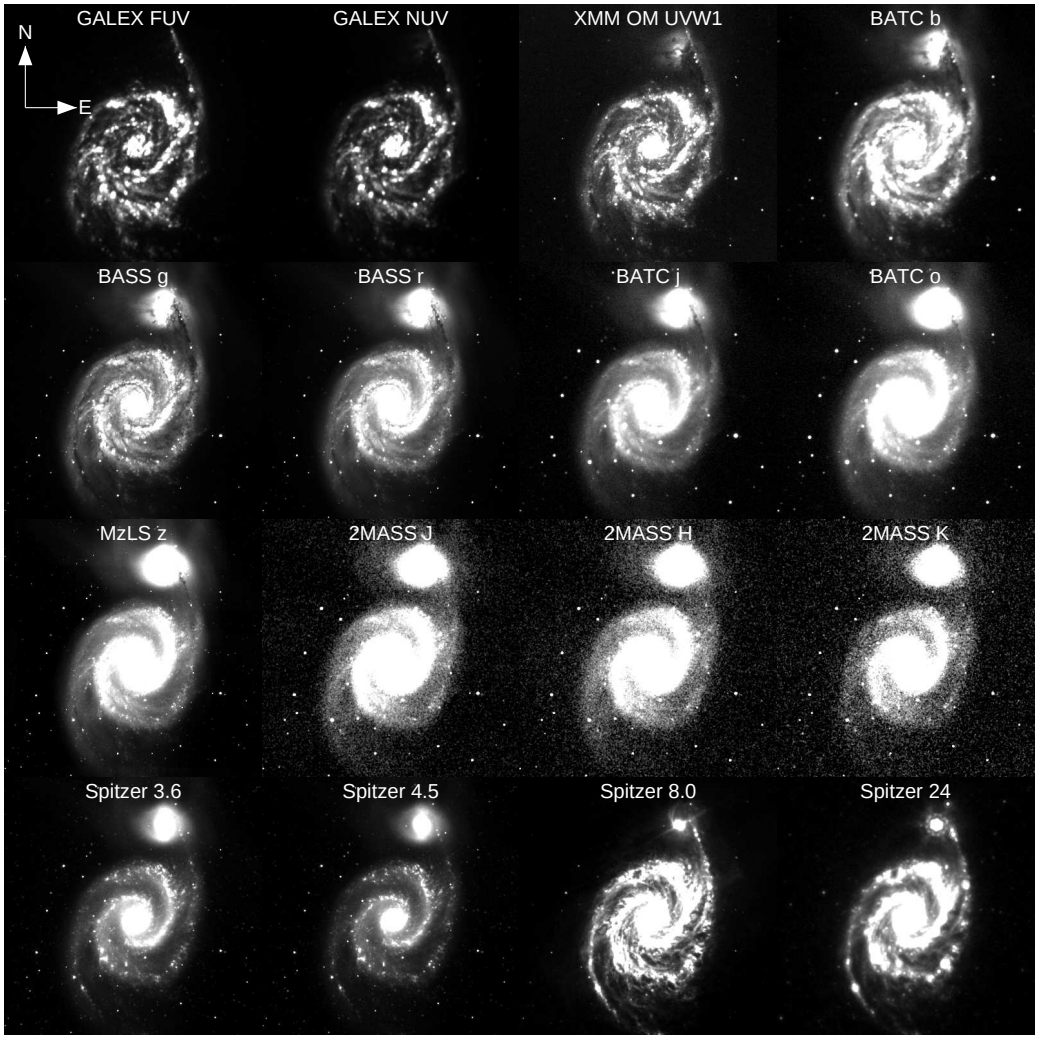

Fig. 1 All processed images from GALEX, XMM-OM, BATC, BASS, MzLS, 2MASS and Spitzer. The image size is about $11' \times 11'$, corresponding to 27×27 kpc at a distance of 8.4 Mpc. The pixel scale is $1.''7$. North is up and east is right.

according to the probability density function of $p(\tau) = 1 - \tanh\left(\frac{8}{\tau} - 6\right)$ with τ^{-1} ranging from 0 to 1.

3.2 SED Fitting Method and Constraint on Dust Extinction

With the spectral library of CSP models as created above, we can construct multi-band model SEDs by convolving the reddened model spectra with filter responses if the intrinsic dust extinction A_V is specified. A χ^2 minimization is performed to estimate the stellar population parameters

$$\chi^2 = \sum_{i=1}^{n} \frac{[F_i^{\rm obs} - c{\times}F_i^{\rm csp}(t, Z, \tau, A_V)]^2}{\sigma_i^2}, \qquad (1)$$

where n is the number of filters used for fitting, $F_i^{\rm obs}$ and σ_i represent the observed flux and corresponding error for the ith filter respectively, c is a scaling factor, and $F_i^{\rm csp}$ is the integrated CSP model flux at specified age t, metallicity Z, star formation timescale τ and dust extinction A_V for the ith filter. The age, metallicity and τ are taken as free parameters, and A_V is constrained by other observational quantities.

As presented in Lin et al. (2013), the dust extinction can be constrained utilizing combined IR and UV observations in order to degrade the parameter degeneracy. The dust attenuation can be estimated by IRX, which is the ratio of total IR (TIR) and FUV luminosities (Meurer et al. 1999; Hao et al. 2011). Here, we use observed IRX to constrain the dust extinction. First, we redden each CSP spectrum for a randomly given A_V (ranging from 0 to 3 mag), assuming the extinction law of Cardelli et al. (1989). Second, the synthetic IRX is calculated through energy conservation, where the TIR luminosity is the flux loss before and after reddening and FUV luminosity is computed by convolving the reddened model with the filter response. Our SED fitting is limited to those models whose

synthesis IRXs are close to the observed IRX within 0.1, considering the measurement uncertainties. The observed IRX is calculated from IRAC 8 μm and MIPS 24 μm luminosities (Calzetti et al. 2005), and is formulated as

$$\mathrm{IRX} = \log\frac{L_{\mathrm{TIR}}}{L_{\mathrm{FUV}}} = \log L(24) + 0.793\log\frac{L_\nu(8)}{L_\nu(24)} + 0.908 - \log L_{\mathrm{FUV}}, \quad (2)$$

where L_{TIR}, L_{FUV} and $L(24)$ are the total IR, FUV and 24 μm luminosities respectively with $L(24) = \nu L_\nu(24)$.

3.3 Error Estimation and Parameter Degeneracy

Two types of parameter error are considered. One is the systematic error (σ_{sys}) caused by our random spectral models and SED fitting method. The systematic error is estimated by fitting a new set of artificial SEDs with the same library of 10^5 spectral models. We produce 5000 new artificial spectra with age, metallicity and τ randomly sampled in the same way as described in Section 3.1. These new spectra are reddened implementing the same Cardelli et al. (1989) extinction law and A_V values are randomly selected from 0 to 3 mag. The IRX of each reddened spectrum is calculated through energy conservation, assuming that the absorbed energy is reradiated by dust in IR. Then we apply the same method to constrain the dust extinction by IRX and the same minimization method as described in Section 3.2 to estimate the stellar population parameters. The standard deviation between the estimated and artificial values for the 5000 spectra is regarded as the systematic error. The systematic error for each parameter varies in different regions of the parameter range, so it is calculated at an interval of 0.1 dex for age and metallicity or 0.1 mag for A_V (especially for age; see Figure 2(d)). Note that the delayed-exponential SFH as adopted in our paper cannot describe the bursts occurring on top of a continuum SFH (Gallazzi & Bell 2009; Zibetti et al. 2009). This limitation artificially reduces the systematic uncertainty on the stellar population parameters.

The other is the random error (σ_{ram}) caused by photometric uncertainty, including both errors of photometry and calibration. The photometric error comes from the flux statistical noise and fluctuation of the sky background. The calibration error is listed in Table 1. The random error of best-fitted parameters is determined by Monte Carlo simulations: (1) for each SED, we generate 100 randomly perturbed SEDs by adding random Gaussian noises to photometric magnitudes assuming that the photometric uncertainties are from normal distributions; (2) best-fitted parameters of these perturbed SEDs are derived through our χ^2 minimization and constraining method of dust extinction; (3) the standard deviation of the 100 fitted values for each parameter is taken as the random error. The final error of each parameter (σ) is the combination of both systematic and random errors, which is expressed as $\sigma = \sqrt{\sigma_{\mathrm{sys}}^2 + \sigma_{\mathrm{ram}}^2}$.

Table 3 Parameter Uncertainties Estimated by Simulations with Different S/Ns

S/N	σ(log age) (log yr)	σ(log Z) (dex)	$\sigma(A_V)$ (mag)
10	0.180	0.097	0.070
20	0.136	0.066	0.059
30	0.121	0.057	0.053
50	0,104	0.046	0.050
100	0.092	0.042	0.042

It is well known that age, metallicity and dust can be degenerate in their effect on broad-band photometric SED. In this work, the IRX is employed to constrain the dust extinction. In addition, the broad-bands ranging from UV to near-IR and intermediate optical bands help to degrade the age-metallicity degeneracy. Actually, the BATC intermediate bands are more sensitive to metallicity. As mentioned in Kong et al. (2000), the BATC near-IR color was used to estimate the metallicity when they performed stellar population synthesis fitting.

We verify whether our method can reliably recover the parameters through Monte Carlo simulations. A total of 5 000 artificial SEDs are created in the same process as described in Section 3.1. These SEDs are scaled to match the mean observed BATC j-band magnitude. Random Gaussian noises are then added to these artificial magnitudes according to a given signal-to-noise ratio (S/N). IRX is simulated through energy conservation as mentioned in the above error estimation. The median S/N is about 20. Figure 2 gives a comparison between the estimated parameters derived by our SED-fitting method and artificial parameters at a typical S/N of 20. The parameter root mean squares (RMSs) for log(Age), log(Z) and A_V at S/N of 20 are about 0.14 dex, 0.07 dex and 0.06 mag, respectively. We also perform Monte Carlo simulations for different S/Ns to represent the RMSs of the best-fit parameters as listed in Table 3. From Figure 2(a)–(c), we can see that age, metallicity and dust extinction are well recovered. As displayed in Figure 2(d) and (e), the age scatter becomes larger as it gets older, while the scatter for metallicity does not change with metallicity. Figure 2(f) shows the difference in metallicity between the artificial and best-fitted values as a function of age and Figure 2(g) depicts the difference in age between the artificial and best-fitted values as a function of metallicity. From these two plots, there is no obvious bias variation in age or metallicity, which indicates that the degeneracy between age and metallicity is not significant.

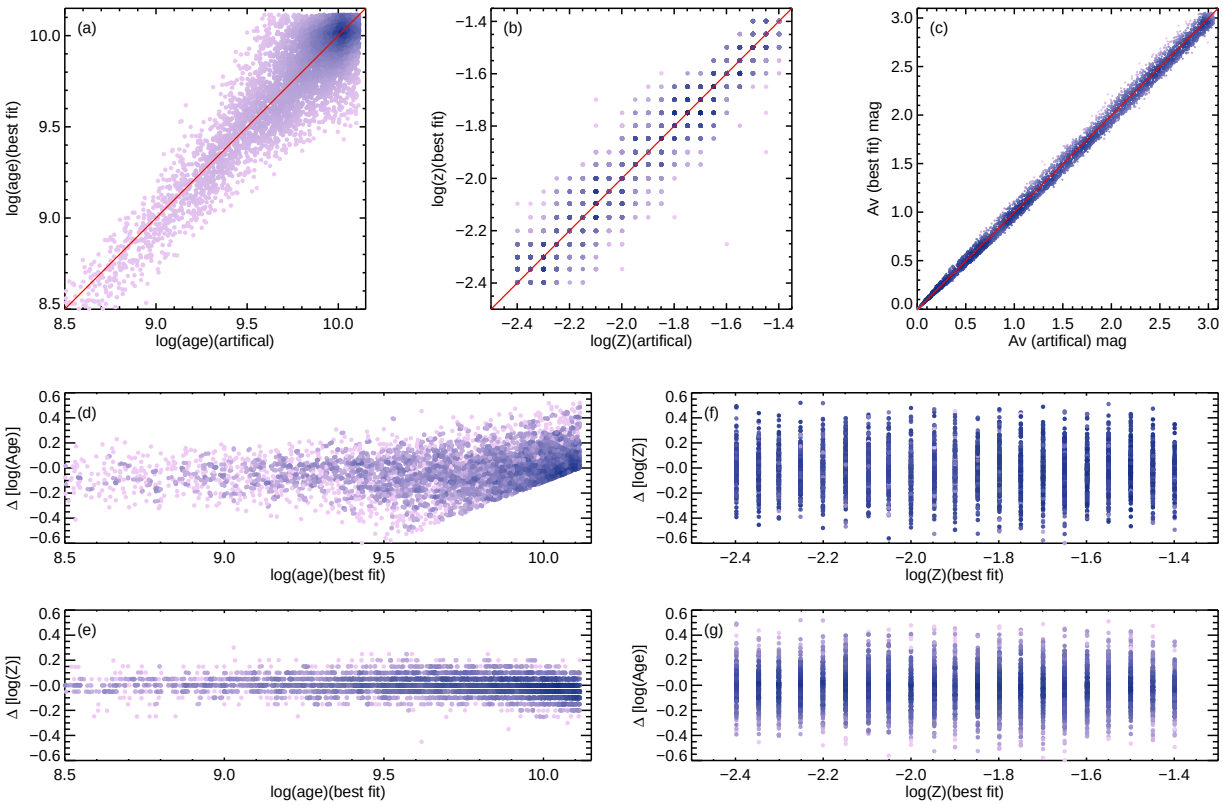

Fig. 2 Comparisons of the best-fitted parameters determined by our SED-fitting method and artificial parameters based on the simulation at a typical S/N of 20. (a) is for age, (b) is for metallicity and (c) is for A_V. The units are yr for age, dex for $\log(Z)$ and mag for A_V. The diagonal solid line in each panel shows the equality between the fitted and artificial parameters. (d) $\Delta \log \mathrm{Age}$ as a function of $\log \mathrm{Age}$. (e) $\Delta \log Z$ as a function of Z. (f) $\Delta \log Z$ as a function of $\log \mathrm{Age}$. (g) $\Delta \log \mathrm{Age}$ as a function of $\log Z$. $\Delta \log Z$ is the difference between artificial metallicity and best-fitted value and $\Delta \log \mathrm{Age}$ is the difference between artificial age and best-fitted value. The color of each point represents the density of the samples.

3.4 Fitting Examples

We choose two pixels at the centers of M51 and NGC 5195 to demonstrate the observed SEDs, fitted parameters and best-fitted templates as plotted in Figure 3. The IRAC 3.6 and 4.5 μm emissions are dominated by starlight, while the 5.6 μm and 8.0 μm are mixed with the emission from polycyclic aromatic hydrocarbons (PAHs). Thus, only IRAC 3.6 and 4.5 μm are considered for stellar population analysis. The BATC a band has a low image quality, so we do not use this band. The BATC e and i bands are also not used due to the strong gaseous emission lines from [O III] and Hα. Finally, there are a total of 23 bands actually included for fitting. At least 15 bands are required to have flux S/N larger than 5. Although not used in fitting, the observed points of BATC a, e, i are still overplotted in Figure 3. In general, our minimization method provides a good match between the model spectrum and observed SED.

4 TWO-DIMENSIONAL AND RADIAL DISTRIBUTIONS OF PARAMETERS

By fitting the observed SED with stellar population synthesis models, we can derive a series of parameters including age, metallicity, dust extinction and stellar mass for each pixel. We extract the multi-band SED pixel by pixel and generate corresponding parameter maps. The pixel scale is about 1.″7, which corresponds to 69 pc at the distance of 8.4 Mpc. It should be noted that all images have been convolved to a PSF FWHM of $\sim$6″, so the actual spatial resolution is larger than 69 pc. After visually examining the parameter maps and multi-band images, we take decl. = 47.°24 as the rough boundary of M51 and NGC 5195.

4.1 Age

The age map in the left panel of Figure 4 affirms that M51 is evidently younger than NGC 5195. The average age of M51 is 4.75 $\pm$ 1.28 Gyr, while that of NGC 5195

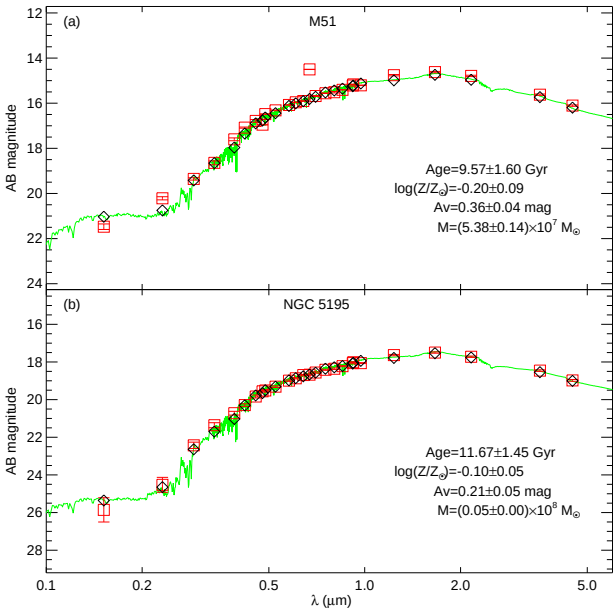

Fig. 3 Two examples of our stellar population synthesis fitting for several selected SEDs. The SEDs are located at the centers of M51 (a) and NGC 5195 (b). The red open squares are observed AB magnitudes with vertical bars indicating the photometric errors. The best-matched model magnitudes are plotted in black diamonds, and corresponding model spectra are drawn in green curves. The fitted age, metallicity, estimated extinction (A_V) by IRX and inferred stellar mass (M) are also displayed in each panel.

is 12.19 ± 1.16 Gyr. If not explicitly specified, the above average values and those in the following of this paper are calculated as mass-weighted ones. In the map of Figure 4, we can see that two young spiral arms extend from the center of M51. The inter-arm regions are relatively older. In order to check whether our age map can reveal the young H II regions, we overlaid the contours of Hα flux density in the left panel of Figure 4. It can be found that all H II regions with strong Hα emission have young ages. However, NGC 5195 lacks such young structures as also indicated in the Hα map. The whole galaxy of NGC 5195 is old.

Radial profiles of stellar population parameters are calculated for each galaxy. The two galaxies are deprojected according to their inclination angles of 20° and 43° and position angles of 10° and 91° for M51 and NGC 5195 (Tully 1974; Spillar et al. 1992), respectively. The radial profile is then obtained by computing azimuthal mass-weighted averages in a set of galactocentric annuli. The radial age profile is presented in the right panel of Figure 4. The center is as old as the surrounding bulge. The bulge of M51 is small, whose size is about $11'' \times 16''$(Lamers et al. 2002). The age decreases steeply from the bulge to the inner disk (about 3 Gyr) at a galactocentric distance of about $25''$(1 kpc). The age gradient in the outer disk with $r > 25''$ is quite flat. Such kinds of two different age gradients in the disk are also found in M33, NGC 628 and M101 (Williams et al. 2009; Zou et al. 2011; Lin et al. 2013). The overall age of NGC 5195 is around 11.5 Gyr and we can also see that there is a mild radial gradient.

4.2 Metallicity

Figure 5 displays the stellar metallicity distributions. The overall average metallicity of M51 is -0.23 ± 0.05 dex, while the average abundance of NGC 5195 is about -0.34 ± 0.05 dex. The metallicity map in Figure 5 affirms that many regions in M51 are super-solar. Most of them are related to spiral arms as demonstrated by the contours of the overlaid Hα intensity map, where massive stars were usually born. The average metallicity $\log(Z/Z_{\odot})$ is 0.05 ± 0.18 dex for these regions. Combining the age and metallicity maps, we can see that the two spiral arms are constituted by young and super-solar stellar populations. Taking the solar abundance of 12 + log(O/H)$_{\odot}$ = 8.69, Croxall et al. (2015) also estimated the gas-phase metallicity to be solar or slightly super-solar using spectra of multiple H II regions in M51. One spiral arm spreads into the east of NGC 5195, standing out compared to the overall poor abundance in this galaxy. The tail of this arm seems to keep the rich chemical composition from the host galaxy of M51, but has a similar old age as NGC 5195.

The right panel of Figure 5 features the radial stellar metallicity profile. The disk presents a metallicity gradient of about -0.016 ± 0.014 dex kpc^{-1}. There are several studies about gas-phase metallicity with spectroscopy of H II regions in M51 (Zaritsky et al. 1994; Bresolin et al. 2004; Moustakas et al. 2010; Croxall et al. 2015). A weak abundance gradient of -0.025 ± 0.008 dex kpc^{-1} was derived by considering the auroral lines of 10 H II regions (Bresolin et al. 2004). Moustakas et al. (2010) obtained two gradient values of –0.038 ± 0.004 dex kpc^{-1} and –0.024 ± 0.004 dex kpc^{-1}. These gradients are calculated by following different metallicity calibration methods. The radial metallicity profile of NGC 5195 features a peak around $r = 50''$, mainly caused by the metal-rich spiral arm originating from M51.

4.3 Dust Extinction

The left panel of Figure 6 shows the dust extinction map. De Looze et al. (2014) derived the FUV attenuation map (see figure 6 in their paper) with a resolution of about $12.1''$ based on FUV and mid- and far-IR observations. If considering $A_{\rm FUV}/A_V \sim 3$ (Fischera & Dopita 2005), our dust extinction map is quite close to theirs. The average extinction A_V of M51 is 0.70 ± 0.04 mag. It is a little high compared to typical Sbc galaxies with $A_V \sim 0.5$

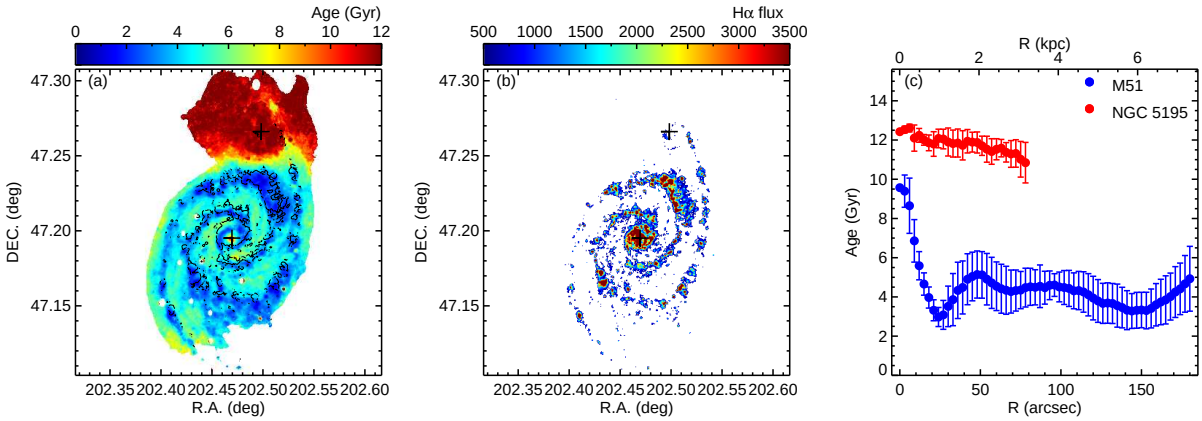

Fig. 4 *Left*: age map. The overplotted contours highlighting spiral arms and H II regions are the Hα isophotes. *Middle*: the Hα intensity map obtained from NASA/IPAC Extragalactic Database. The centers of M51 and NGC 5195 are displayed with pluses. *Right*: deprojected radial mass-weighted age profiles. The error bars are the standard deviations at different galactocentric annuli.

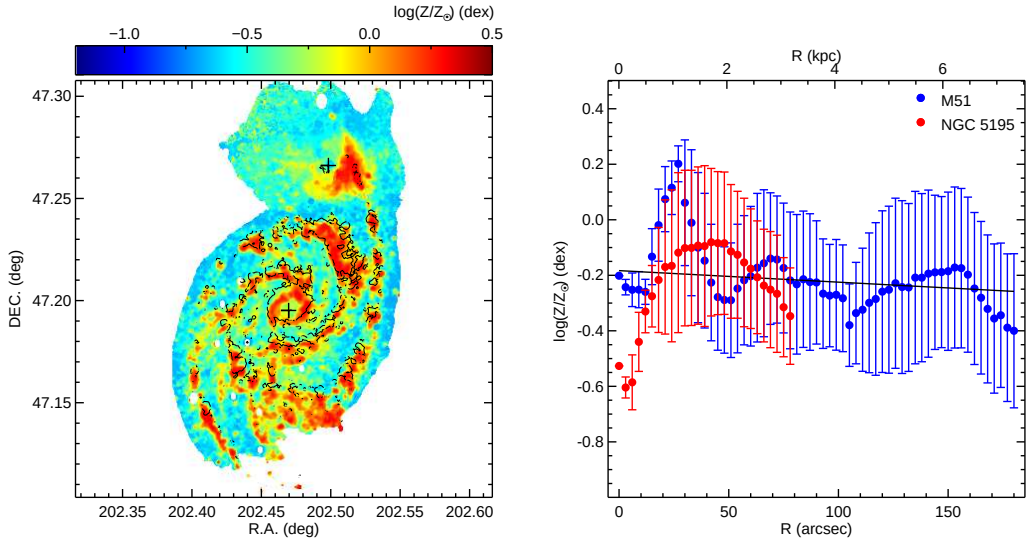

Fig. 5 *Left*: metallicity map in $\log(Z/Z_{\odot})$. The overplotted contours indicate the Hα intensity map. The centers of M51 and NGC 5195 are displayed with pluses. *Right*: deprojected radial mass-weighted metallicity profiles. The error bars are the standard deviations at different galactocentric annuli. The black solid line traces the best-linear fit in M51 using the radial mass-weighted metallicity profiles.

mag (Boselli et al. 2003; Muñoz-Mateos et al. 2009). We overlay the contours of the Herchel PACS 70 μm intensity map as displayed in the middle of Figure 6 onto the dust extinction map. It can be seen that most of the 70 μm observational features coincide with the substructures with high dust extinction. Although the outer spiral arms present low IR luminosity, the dust extinction is still high due to residing dust lanes and fewer illuminating young stars. Most of the regions with high extinction are located at the inner part of spiral arms.

The radial extinction profiles are graphed in the right panel of Figure 6. The dust attenuation in the bulge of M51 is smaller than the surrounding inner disk. It increases steadily from the center and peaks at $r = 25''$ (1.0 kpc), forming a young, metal-rich and dusty ring. The outer disk presents a descending gradient with A_V varying from 1.0 to 0.5 mag. The average dust attenuation of NGC 5195 is 0.65 ± 0.04 mag. In this galaxy, the central region is dusty, while the outer part is almost free of dust. The nucleus of NGC 5195 has a maximum extinction up to about 1.67 mag. Spillar et al. (1992) has estimated the extinction in the center to be as high as $A_V = 2.0$ mag. Despite lack of star formation, for NGC 5195, it has a relatively high (29 ± 3 K) dust temperature in the nuclear region, which is associated with an active star forming galaxy under normal circumstances (Mentuch Cooper et al. 2012). Although

there is no obvious recent star formation apparent in the Hα intensity map, this kind of dusty and relatively hot center can be heated by the strong radiation field from high stellar densities (Engelbracht et al. 2010). In addition, the tip of the overlaid spiral arm from M51 is almost dust-free with $A_V \sim 0.2$ mag. There might be some mechanisms leading to the dust loss.

4.4 Stellar Mass Surface Density

The map of stellar mass surface density featured in the left of Figure 7 follows the K_s-band morphology, which is regarded as a good tracer of stellar mass. The bulge is dominated by low-mass stars still on the main sequence contributing most of the total stellar mass. The mass is enhanced along the spiral arms in M51. The stellar mass surface density radially decreases from the central regions of both galaxies to the outskirts (see the right panel of Fig. 7). The radial profiles display distinct bulge and disk components. The core region of NGC 5195 is denser than M51. The total stellar mass of M51 is $2.97 \pm 0.23 \times 10^{10}\ M_{\odot}$ and that of NGC 5195 is $2.90 \pm 0.11 \times 10^{10}\ M_{\odot}$. The mass ratio is close to 1:1. The stellar mass of NGC 5195 might be overestimated, because one of the spiral arms extending from M51 overlays this galaxy. Table 4 lists the average parameter values for both M51 and NGC 5195.

4.5 Comparing with the Work of Mentuch Cooper et al. (2012)

For the M51-NGC 5195 system, Mentuch Cooper et al. (2012) also studied the spatially-resolved properties of this system from the multi-wavelength photometric data. In their work, the stellar population and dust properties were independently determined using different bands. The optical and near-IR bands were applied to model the stellar population and mid- and far-IR bands were utilized to obtain the dust parameters. For the stellar population synthesis, they adopted a sum of a continuous population modeled as an exponentially decreasing function of time and an additional burst of star formation modeled as a tau-exponential with timescale of τ = 100 Myr. The main goal was to determine when the recent bust of star formation occurred. They indeed obtained a starburst with age of about 370–480 Myr ago, consistent with the simulations. We adopt a single exponentially delayed SFH and give average age of $\sim$ 2–3 Gyr for the H II regions. The age is older than the time of the recent encounter, because the observed SED includes the underlying older disk stellar populations and thus the derived age is the combination of the stars that recently bursted and old disk stars.

However, the issue of parameter degeneracy should be more serious in Mentuch Cooper et al. (2012), because their stellar population modeling was based on only seven bands from optical B to 2MASS K_s bands and they considered two components of star formation histories simultaneously. In our work, we gather a total of 26 bands with wavelength ranging from 1500 Å to 4.5 µm. The BATC intermediate colors can be used to constrain the metallicity well. The observed IRX is adopted to constrain the dust extinction. In this way, the parameter degeneracy is considerably relieved. In addition, the spatial resolution of our data is about 6″, about 5 times better than the one in Mentuch Cooper et al. (2012), so that we can examine the parameter distributions in more details. For example, Mentuch Cooper et al. (2012) gave a flat age profile for both M51 and NGC 5195 ($\sim$ 7 – 10 Gyr). In our age map, we can see an older bulge and younger disk and the age gradient is steeper in the inner region and becomes shallower in the outer region, which are common in many spiral galaxies. Due to the lack of UV data, Mentuch Cooper et al. (2012) claimed that the dust extinction was modestly underestimated ranging from 0.5 mag in the center to 0.2 mag in the outer region. Our dust extinction distribution presents a decreasing gradient ranging from 1.0 to 0.5 mag, which is consistent with the results of De Looze et al. (2014). Note that the extent of the radial profiles as computed in our work is $\sim$ 7.5 kpc in terms of a distance of 8.4 Mpc, smaller than that of Mentuch Cooper et al. (2012) ($\sim$ 12 kpc).

5 DISCUSSION

5.1 Pseudobulge of M51 and Secular Evolution

Recent observations indicate that bulges in nearby disk galaxies are complicated and there are at least two types: classical bulges and pseudobulges. Classical bulges are dominated by random motions and old stars. Pseudobulges are characterized by rotating motion, active star formation, nuclear bar, ring and/or spiral, and near-exponential surface brightness profile (Kormendy & Kennicutt 2004).

The Sérsic index of M51's bulge is about 0.55 ± 0.07 (Fisher & Drory 2010). It is less than 2.0, which is commonly regarded as a separation between classical bulges and pseudobulges. From high-resolution images and our parameter maps, we can see resolved nuclear spirals. In addition, it is reported that there is a small bar in the bulge. Menéndez-Delmestre et al. (2007) measured the bar fraction and found that the bulge of M51 has an inner nuclear bar with a major axis length of about 16″ and an orientation of about 139°. From our radial parameter profiles as showcased in Section 4, the bulge is metal-poorer and less dusty than the surrounding area. There is clear Hα emission in the BATC i band as featured in panel (a) of Figure 3, implying some extent of star formation, although a part of the Hα emission is

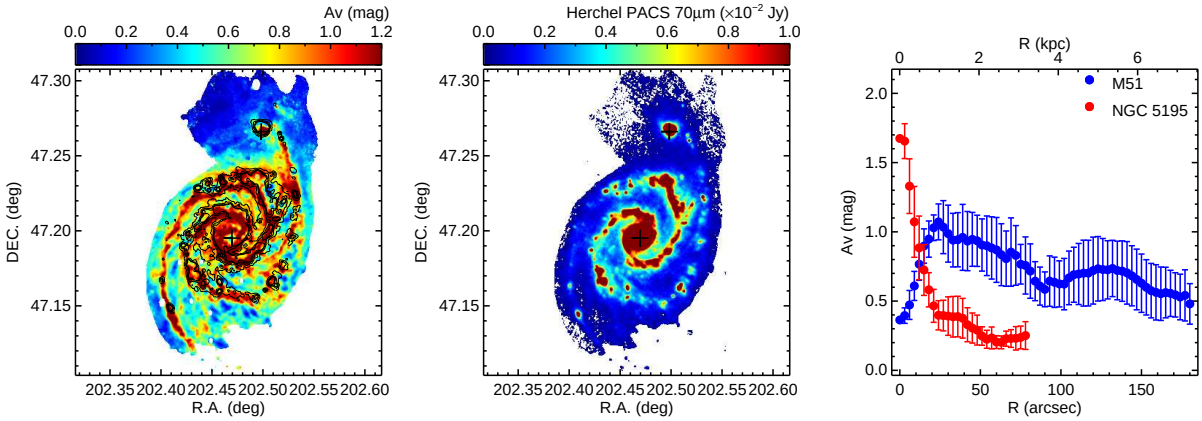

Fig. 6 *Left*: dust extinction map in A_V. The overplotted contours signify the regions with strong Herschel PACS 70 μm radiation. The centers of M51 and NGC 5195 are displayed with pluses. *Middle*: intensity map of Herschel PACS 70 μm in Jy sr^{-1}. *Right*: deprojected radial mass-weighted extinction profiles. The error bars are the standard deviations at different galactocentric annuli.

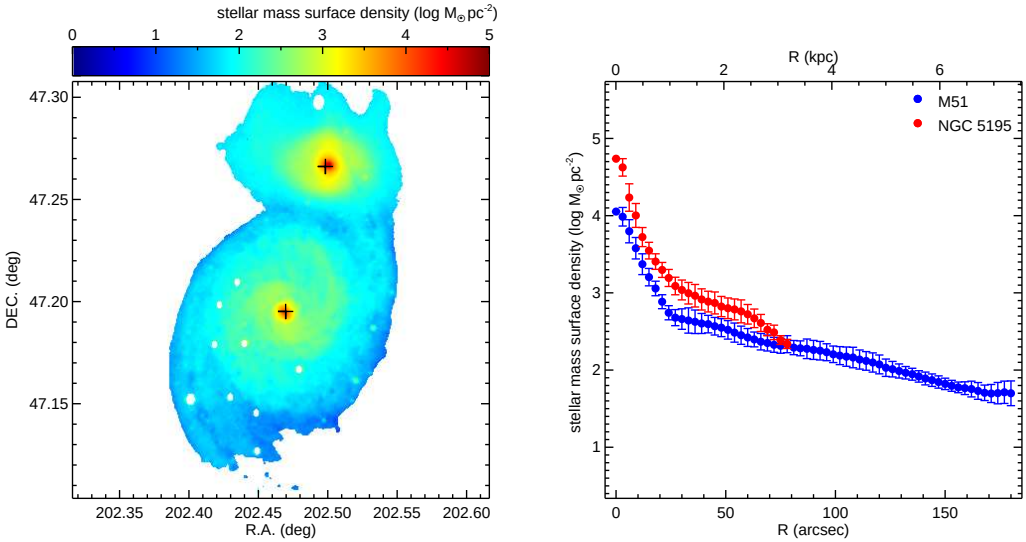

Fig. 7 *Left*: stellar mass surface density map. The centers of M51 and NGC 5195 are displayed with pluses. *Right*: deprojected radial stellar mass surface density profiles. The error bars are the standard deviations at different galactocentric annuli.

Table 4 Average Parameter Values for M51 and NGC 5195

	Age (Gyr)	$\log(Z/Z_\odot)$ (dex)	A_V (mag)	Stellar mass[a] ($M_\odot$)
M51	4.74 ± 1.28	-0.23 ± 0.05	0.70 ± 0.04	$2.97 \pm 0.23 \times 10^{10}$
NGC 5195	12.19 ± 1.16	-0.34 ± 0.05	0.65 ± 0.04	$2.90 \pm 0.11 \times 10^{10}$

[a] Stellar mass is calculated by summing the masses of all pixels belonging to the galaxy.

contributed by AGN (Goad et al. 1979; Moustakas et al. 2010). Gas inflow could dilute the metallicity and induce more star formation. A rather chaotic distribution of dust lanes can be found in high-resolution images of the central region of M51 taken by the Hubble Space Telescope (HST), which also indicates that M51 is transporting gas to the nucleus (Grillmair et al. 1997). The nucleus of M51 has an average rotation velocity of about 240 ± 20 km s^{-1} (Kormendy et al. 2010), and the velocity dispersion is about 96.0 ± 8.7 km s^{-1} (Ho et al. 2009). Fisher & Drory (2010) measured the $3.6-8.0$ μm color as a rough estimate of the specific SFR and reported that the bulge of M51 is slightly active. A group of 30 bright massive stars found in HST images also implies that there is ongoing massive star formation (Lamers et al. 2002). All above characteristics hint that the bulge of M51 is a slightly active pseudobulge.

Unlike classical bulges that are typically merger-built, galaxies form pseudobulges via processes in the secular evolution of the galactic disk (Kormendy & Kennicutt 2004; Fisher & Drory 2008; Fisher et al. 2009; Fisher & Drory 2010). The growth of a pseudobulge is driven by the nonaxisymmetry of bars, ovals and/or spiral structures in the disk that can cause gas infall, building up a central mass concentration, and hence trigger star formation. It is possible that the pseudobulge of M51 was formed by the secular evolution of the disk driven by the nonaxisymmetric potential of spiral arms and small bar. Since M51 and NGC 5195 are currently interacting, extremely gas-rich accretion events, gravitational encounters and interactions also have an effect on forming the pseudobulge (Kormendy & Kennicutt 2004; Fisher & Drory 2008).

5.2 Evolution Effect of the Galaxy Interaction

The M51–NGC 5195 system is an interacting galaxy pair. They underwent an encounter 300–500 Myr ago, which is inferred from kinematic and hydrodynamic modelings (Salo & Laurikainen 2000; Dobbs et al. 2010). There are two grand-design spiral arms in the disk of M51. The parameter maps in our paper affirm that these two spectacular spiral arms starting from the bulge are dominated by younger, metal-richer and less dusty stellar populations. The spiral arms exhibit considerable H II regions, supporting that there is ongoing star formation across the galaxy. It was stated in Nikola et al. (2001) that the outlying spiral substructures are attributed to material clumping formed by the galactic interaction. The radial age profile of M51 presents a flat gradient in the outer disk. The abundance gradient of the stellar content is about -0.016 dex kpc^{-1}, close to the gas-phase metallicity gradient. It is much lower than other typical isolated galaxies (Zaritsky et al. 1994; Lin et al. 2013). Salo & Laurikainen (2000) implied that there might be multiple encounters between M51 and NGC 5195. It is possible that those multiple close encounters made the age and metallicity gradients flatten (Kewley et al. 2006).

Further, as seen from the age, metallicity and A_V maps, there are more substructures in the north spiral arms filled with young, metal-rich and dusty stellar populations. They are also present in the Hα intensity map. Kaleida & Scowen (2010) identified and measured 120 single-aged stellar associations. They found that there is an enhancement in the number of stellar associations in the northern spiral arm of M51. The enhanced star formation in the north arms is possibly induced by the galactic interaction.

NGC 5195 is a post-starburst galaxy. The old age and a lack of Hα emission indicate that there is no recent star formation. It is interesting to find that the bulge of NGC 5195 is fairly dusty in Figure 6. The dust is most likely to be heated by the evolved stellar populations, since the stellar mass is highly concentrated in the galaxy core as demonstrated in the stellar mass distributions of Figure 7. It is exciting to find that the tip of the north-east spiral arm extending from M51 to NGC 5195 is almost free of dust but still keeps the high metallicity of the original arm (see maps in Figs. 5 and 6). By contrast, the other spiral arms in the opposite direction present both high metallicity and large dust attenuation. It is possible that the close encounters of these two galaxies made the dust in the north-east arm be accreted by NGC 5195. As analyzed in Mentuch Cooper et al. (2012), when the two galaxies were at the stages of close encounters, tidal forces likely lead to high accretion rates of gas and dust that caused starburst. But as the galaxies moved apart, the tidal forces were reduced and gas was exhausted so that the star formation ceased in NGC 5195. It is also possible that the growth of the stellar bulge in NGC 5195 resulted in a stable disk causing the star formation to cease (termed as "morphological quenching", Martig et al. 2009), as we can see that most of the stellar mass and dust are concentrated in the bulge.

In conclusion, there are a lot of hints indicating that the bulge of M51 is a pseudobulge formed through secular evolution. The gravitational asymmetry drives the gas inflow and leads to the slow growth of the pseudobulge. The galaxy interaction enables more enhanced star formation in the north arms and yields possible gas inflow and material exchange between M51 and NGC 5195. Both secular evolution and galaxy interaction might play important roles in the current evolution of this interacting system.

6 SUMMARY

Nearby galaxies such as the M51–NGC 5195 galaxy pair are ideal objects to examine the stellar population, galaxy interaction and galaxy evolution in great details. Multi-wavelength photometric data ranging from UV to IR provide spatially resolved SEDs for nearby galaxies. Through fitting the observed SED with EPS models, we can reliably derive a series of stellar population properties. Although similar work of Mentuch Cooper et al. (2012) was carried out to present spatially-resolved stellar population analysis for this interacting system, the stellar population modeling of their work is based on only a few bands and two components of SFHs. There are serious parameter degeneracies in Mentuch Cooper et al. (2012). In this paper, we revisit the stellar population synthesis analysis with a higher spatial resolution and much more bands ranging from UV and near-IR in order to derive more reliable parameters.

We collect a total of 28 deep images of the M51–NGC 5195 system from GALEX, XMM-OM, BATC, BASS, MzLS, 2MASS and Spitzer with wavelength ranging from 1500 Å to 24 μm and a lowest spatial resolution of 6″. These data are processed by a dedicated pipeline, which includes the process of subtracting sky background, matching to a common resolution of 6″ and a pixel scale of 1.″7, and masking foreground stars. The stellar population synthesis models of BC03 with the Chabrier (2003) IMF, Padova 1994 evolutionary tracks and delayed-exponential SFH are adopted in this paper. From SED fitting, we obtained the two-dimensional distribution and radial profiles of a series of parameters including age, metallicity, dust extinction and stellar mass. The dust extinction is constrained by the observed IRX.

The average mass-weighted age, metallicity in $\log(Z/Z_{\odot})$ and dust extinction in A_V for M51 is 4.74±1.28 Gyr, -0.23 ± 0.05 dex and 0.70 ± 0.04 mag, respectively. Those for NGC 5195 are 12.19 ± 1.16 Gyr, -0.34 ± 0.05 dex and 0.65 ± 0.04 mag. NGC 5195 is much older. The stellar masses are $2.97 \pm 0.23 \times 10^{10}$ $M_{\odot}$ for M51 and $2.90 \pm 0.11 \times 10^{10}$ $M_{\odot}$ for NGC 5195. The mass ratio is close to 1:1. The grand-design spiral arms can be clearly seen in almost all parameter maps. Generally, they are young, metal-rich, dusty and massive. The enhanced star formation in the north arms is possibly induced by the galaxy interaction. However, except for the spiral arm extending from M51 into NGC 5195, the stellar population properties of NGC 5195 are quite featureless. There are very small radial age and metallicity gradients in the outer disk of M51. The metallicity gradient is about –0.016 dex kpc^{-1}, close to the gas-phase one. It is possible that the galaxy interaction between M51 and NGC 5195 makes the gradients flatter than other isolated nearby galaxies. The core region of NGC 5195 is dusty and has exceptionally high dust temperatures. The dust content might be accreted from M51 through close encounters, since the tip of the superposed spiral arm from M51 seems free of dust. The large amount of old stellar populations in the core of NGC 5195 can heat the dust. The secular evolution and galaxy interaction might jointly lead the current evolution and structure growth of the M51–NGC 5195 system.

Acknowledgements We thank the anonymous referee for his/her thoughtful comments and insightful suggestions that improved our paper greatly. This work is supported by Major Program of National Natural Science Foundation of China (No. 11890691). This work is also supported by the National Basic Research Program of China (973 Program; Grant No. 2017YFA0402600), the National Natural Science Foundation of China (NSFC; Grant Nos. 11433005, 11673027, 11733007, 11973038, 11320101002 and 11421303), and the External Cooperation Program of Chinese Academy of Sciences (Grant No. 114A11KYSB20160057). The 60/90 cm Schmidt telescope at the Xinglong Station of National Astronomical Observatories, Chinese Academy of Sciences is jointly operated and administrated by the National Astronomical Observatories, Chinese Academy of Sciences and Center for Astronomical Mega-Science, Chinese Academy of Sciences.

This work is based in part on observations made with the Spitzer Space Telescope, which is operated by the Jet Propulsion Laboratory, California Institute of Technology under a contract with NASA. This publication makes use of data products from the Two Micron All Sky Survey, which is a joint project of the University of Massachusetts and the Infrared Processing and Analysis Center/California Institute of Technology, funded by the National Aeronautics and Space Administration and the National Science Foundation.

BASS is a collaborative program between the National Astronomical Observatories, Chinese Academy of Sciences and Steward Observatory of the University of Arizona. It is a key project of the Telescope Access Program (TAP), which has been funded by National Astronomical Observatories, Chinese Academy of Sciences (the Strategic Priority Research Program “The Emergence of Cosmological Structures” grant No. XDB09000000), and the Special Fund for Astronomy from the Ministry of Finance. BASS is also supported by the External Cooperation Program of Chinese Academy of Sciences (Grant No. 114A11KYSB20160057) and the National Natural Science Foundation of China (Grant No. 11433005).

References

Bertin, E. 2010, SWarp: Resampling and Co-adding FITS Images Together

Boselli, A., Gavazzi, G., & Sanvito, G. 2003, A&A, 402, 37

Bresolin, F., Garnett, D. R., & Kennicutt, Robert C., J. 2004, ApJ, 615, 228

Bruzual, A. G. 2007, in IAU Symposium, 241, Stellar Populations as Building Blocks of Galaxies, eds. A. Vazdekis & R. Peletier, 125

Bruzual A., G., & Charlot, S. 1993, ApJ, 405, 538

Bruzual, G., & Charlot, S. 2003, MNRAS, 344, 1000

Burstein, D., Hester, J. J., Windhorst, R. A., et al. 1994, in American Astronomical Society Meeting Abstracts, 185, 41.10

Calzetti, D., Kennicutt, R. C., J., Bianchi, L., et al. 2005, ApJ, 633, 871

Cardelli, J. A., Clayton, G. C., & Mathis, J. S. 1989, ApJ, 345, 245

Chabrier, G. 2003, PASP, 115, 763

Chambers, K. C., Magnier, E. A., Metcalfe, N., et al. 2016, arXiv e-prints, arXiv:1612.05560
Charlot, S., & Bruzual A, G. 1991, ApJ, 367, 126
Cortés, J. R., Kenney, J. D. P., & Hardy, E. 2006, AJ, 131, 747
Croxall, K. V., Pogge, R. W., Berg, D. A., Skillman, E. D., & Moustakas, J. 2015, ApJ, 808, 42
Dark Energy Survey Collaboration, Abbott, T., Abdalla, F. B., et al. 2016, MNRAS, 460, 1270
De Looze, I., Fritz, J., Baes, M., et al. 2014, A&A, 571, A69
Dey, A., Schlegel, D. J., Lang, D., et al. 2019, AJ, 157, 168
Dobbs, C. L., Theis, C., Pringle, J. E., & Bate, M. R. 2010, MNRAS, 403, 625
Eldridge, J. J., & Stanway, E. R. 2009, MNRAS, 400, 1019
Engelbracht, C. W., Hunt, L. K., Skibba, R. A., et al. 2010, A&A, 518, L56
Fan, X., Burstein, D., Chen, J. S., et al. 1996, AJ, 112, 628
Feldmeier, J. J., Ciardullo, R., & Jacoby, G. H. 1997, ApJ, 479, 231
Fioc, M., & Rocca-Volmerange, B. 1997, A&A, 500, 507
Fischera, J., & Dopita, M. 2005, ApJ, 619, 340
Fisher, D. B., & Drory, N. 2008, AJ, 136, 773
Fisher, D. B., & Drory, N. 2010, ApJ, 716, 942
Fisher, D. B., Drory, N., & Fabricius, M. H. 2009, ApJ, 697, 630
Gaia Collaboration, Brown, A. G. A., Vallenari, A., et al. 2016, A&A, 595, A2
Gallazzi, A., & Bell, E. F. 2009, ApJS, 185, 253
Goad, J. W., de Veny, J. B., & Goad, L. E. 1979, ApJS, 39, 439
Grillmair, C. J., Faber, S. M., Lauer, T. R., et al. 1997, AJ, 113, 225
Hao, C.-N., Kennicutt, R. C., Johnson, B. D., et al. 2011, ApJ, 741, 124
Ho, L. C., Greene, J. E., Filippenko, A. V., & Sargent, W. L. W. 2009, ApJS, 183, 1
Jarrett, T. H., Chester, T., Cutri, R., Schneider, S. E., & Huchra, J. P. 2003, AJ, 125, 525
Kaleida, C., & Scowen, P. A. 2010, AJ, 140, 379
Kennicutt, Robert C., J., Bresolin, F., & Garnett, D. R. 2003, ApJ, 591, 801
Kewley, L. J., Geller, M. J., & Barton, E. J. 2006, AJ, 131, 2004
Kong, X., Zhou, X., Chen, J., et al. 2000, AJ, 119, 2745
Kormendy, J., Drory, N., Bender, R., & Cornell, M. E. 2010, ApJ, 723, 54
Kormendy, J., & Kennicutt, Robert C., J. 2004, ARA&A, 42, 603
Kotulla, R., Fritze, U., Weilbacher, P., & Anders, P. 2009, MNRAS, 396, 462
Kuntz, K. D., Harrus, I., McGlynn, T. A., Mushotzky, R. F., & Snowden, S. L. 2008, PASP, 120, 740
Lamers, H. J. G. L. M., Panagia, N., Scuderi, S., et al. 2002, ApJ, 566, 818
Leitherer, C., Schaerer, D., Goldader, J. D., et al. 1999, ApJS, 123, 3
Li, J.-L., Zhou, X., Ma, J., & Chen, J.-S. 2004a, ChJAA (Chin. J. Astron. Astrophys.), 4, 143
Li, J., Ma, J., Zhou, X., et al. 2004b, A&A, 420, 89
Lin, L., Zou, H., Kong, X., et al. 2013, ApJ, 769, 127
Maraston, C. 2005, MNRAS, 362, 799
Martig, M., Bournaud, F., Teyssier, R., & Dekel, A. 2009, ApJ, 707, 250
Martin, D. C., Fanson, J., Schiminovich, D., et al. 2005, ApJL, 619, L1
Mason, K. O., Breeveld, A., Much, R., et al. 2001, A&A, 365, L36
Menéndez-Delmestre, K., Sheth, K., Schinnerer, E., Jarrett, T. H., & Scoville, N. Z. 2007, ApJ, 657, 790
Mentuch Cooper, E., Wilson, C. D., Foyle, K., et al. 2012, ApJ, 755, 165
Meurer, G. R., Heckman, T. M., & Calzetti, D. 1999, ApJ, 521, 64
Morrissey, P., Conrow, T., Barlow, T. A., et al. 2007, ApJS, 173, 682
Moustakas, J., Kennicutt, Robert C., J., Tremonti, C. A., et al. 2010, ApJS, 190, 233
Muñoz-Mateos, J. C., Gil de Paz, A., Boissier, S., et al. 2009, ApJ, 701, 1965
Nikola, T., Geis, N., Herrmann, F., et al. 2001, ApJ, 561, 203
Oke, J. B., & Gunn, J. E. 1983, ApJ, 266, 713
Roškar, R., Debattista, V. P., Stinson, G. S., et al. 2008, ApJL, 675, L65
Salo, H., & Laurikainen, E. 2000, MNRAS, 319, 393
Schlegel, D. J., Finkbeiner, D. P., & Davis, M. 1998, ApJ, 500, 525
Silva, D. R., Blum, R. D., Allen, L., et al. 2016, in American Astronomical Society Meeting Abstracts, 228, 317.02
Skrutskie, M. F., Cutri, R. M., Stiening, R., et al. 2006, AJ, 131, 1163
Spillar, E. J., Oh, S. P., Johnson, P. E., & Wenz, M. 1992, AJ, 103, 793
Toomre, A., & Toomre, J. 1972, ApJ, 178, 623
Tully, R. B. 1974, ApJS, 27, 449
Walter, F., Brinks, E., de Blok, W. J. G., et al. 2008, AJ, 136, 2563
Werner, M. W., Roellig, T. L., Low, F. J., et al. 2004, ApJS, 154, 1
White, S. D. M., & Rees, M. J. 1978, MNRAS, 183, 341
Williams, B. F., Dalcanton, J. J., Dolphin, A. E., Holtzman, J., & Sarajedini, A. 2009, ApJL, 695, L15
York, D. G., Adelman, J., Anderson, John E., J., et al. 2000, AJ, 120, 1579
Zacharias, N., Finch, C., Girard, T., et al. 2010, AJ, 139, 2184
Zaritsky, D., Kennicutt, Robert C., J., & Huchra, J. P. 1994, ApJ, 420, 87
Zhou, X., Jiang, Z.-J., Xue, S.-J., et al. 2001, ChJAA (Chin. J. Astron. Astrophys.), 1, 372
Zibetti, S., Charlot, S., & Rix, H.-W. 2009, MNRAS, 400, 1181
Zou, H., Zhang, W., Yang, Y., et al. 2011, AJ, 142, 16
Zou, H., Zhou, X., Fan, X., et al. 2017a, PASP, 129, 064101
Zou, H., Zhang, T., Zhou, Z., et al. 2017b, AJ, 153, 276
Zou, H., Zhang, T., Zhou, Z., et al. 2018, ApJS, 237, 37